

JGR Space Physics

RESEARCH ARTICLE

10.1029/2019JA026556

Key Points:

- Power-weighted wave normal angles (WNAs) of fast magnetosonic (MS) waves mainly range from 87°–89° near the geomagnetic equator, ~85° at off-equatorial region
- The wave normal angles are distributed as a mixture of two Gaussian distributions, and the tangent of it decreases as a Kappa distribution function with increasing geomagnetic latitude
- The statistical results provide valuable information for incorporation into future simulations of radiation belt particle dynamics

Correspondence to:

P. Zuo,
pbzuo@hit.edu.cn

Citation:

Zou, Z., Zuo, P., Ni, B., Wei, F., Zhao, Z., Cao, X., et al. (2019). Wave normal angle distribution of fast magnetosonic waves: A survey of Van Allen Probes EMFISIS observations. *Journal of Geophysical Research: Space Physics*, 124, 5663–5674. <https://doi.org/10.1029/2019JA026556>

Received 28 JAN 2019

Accepted 26 JUN 2019

Accepted article online 17 JUL 2019

Published online 30 JUL 2019

Wave Normal Angle Distribution of Fast Magnetosonic Waves: A Survey of Van Allen Probes EMFISIS Observations

Zhengyang Zou¹ , Pingbing Zuo¹ , Binbin Ni^{2,3} , Fengsi Wei¹, Zhengyu Zhao^{1,2}, Xing Cao² , Song Fu² , and Xudong Gu² 

¹Institute of Space Science and Applied Technology, Harbin Institute of Technology, Shenzhen, China, ²Department of Space Physics, School of Electronic Information, Wuhan University, Wuhan, Hubei, China, ³CAS Center for Excellence in Comparative Planetology, Hefei, China

Abstract Using Van Allen Probe Electric and Magnetic Field Instrument Suite and Integrated Science (EMFISIS) wave observations from September 2012 to May 2018, we statistically investigate the distributions of power-weighted wave normal angle (WNA) of fast magnetosonic (MS) waves from $L = 2\text{--}6$ within $\pm 15^\circ$ geomagnetic latitudes. The spatial distributions show that the MS WNAs are mainly confined within 87°–89° near the geomagnetic equator and decrease with increasing magnetic latitude. Further quantitative investigation demonstrates that the WNAs normally distribute as a mixture of two Gaussian distributions ranging from 85° to 88°, and the tangent of it can decrease as a Kappa distribution function when the waves propagate to higher latitudes. Our study completes the survey of spatial distributions of MS WNAs and provides quantitative dependence of the WNA distribution on the magnetic latitude in the inner magnetosphere, which can be readily useful in future global simulations of radiation belt particle dynamics.

1. Introduction

Fast mode magnetosonic (MS) waves, also known as “equatorial noise,” are electromagnetic emissions that occur characteristically within $\pm 3^\circ$ of the geomagnetic latitudes (λ) at a broad range of L-shells from 2 to 8 both inside and outside the plasmapause (PP; e.g., Russell et al., 1970; Santolík et al., 2002; Shprits et al., 2013; Meredith et al., 2008; Chen & Thorne, 2012; Balikhin et al., 2015). Excited by the ring distribution of energetic protons, MS waves are initially linearly polarized with frequencies ranging from the proton cyclotron frequency (f_{cp}) to the lower hybrid frequency (f_{LHR}) and propagate in both radial and azimuthal directions in a manner quasi-perpendicular to the ambient magnetic field (e.g., Chen & Thorne, 2012; Xiao et al., 2015). Recent studies reported that MS waves occasionally consist of frequency harmonic structures (e.g., Artemyev et al., 2015; Balikhin et al., 2015) and discrete wave elements with rising tone (e.g., Boardsen et al., 2014; Fu et al., 2014) or “Zipper-like” periodic structure (Li et al., 2017). It is reported that their wave amplitude can substantially decay along with the increase of the geomagnetic latitude (λ) at off-equatorial region (Tsurutani et al., 2014; Ma et al., 2013, 2016).

With a capability to resonant with energetic electrons and protons in the outer radiation belt via Landau resonance (Horne et al., 2007) and transit time effect (Bortnik & Thorne, 2010; Li et al., 2014; Fu et al., 2016), MS waves are regarded as a viable candidate to influence the dynamics of the radiation belt particles. Recent investigation has further confirmed that off-equatorial MS waves can also efficiently transport radiation belt electrons from high to intermediate pitch angles and consequently form electron butterfly pitch angle distributions (Ni et al., 2018). For a large amount of previous studies that have evaluated the scattering effects of MS waves on radiation belt electrons and protons (e.g., Bortnik & Thorne, 2010; Li et al., 2014; Fu et al., 2016; Ni et al., 2017, 2018; Hua et al., 2019), the wave normal angle (WNA) distribution is an essential input for computations and typically adopted as a Gaussian function with a central peak at 89° or 89.5°, mainly due to their characteristically nearly perpendicular propagation with respect to the background magnetic field. More recently, using test particle simulations to estimate the MS waves-induced electron diffusion effect, Mourenas et al. (2013) and Lei et al. (2017) found that compared to the waves with WNA = 89.5°, the MS emissions with WNA = 87° have a much stronger efficiency to scatter the near-90° pitch angle electrons. Those studies demonstrate that the distribution of WNA plays a critical role in quantification of

the electron scattering effect of MS waves, and even a small variation in WNA may result in a considerable change in the scattering rates. However, to the best of our knowledge, the WNA model of MS waves has not been well established so far.

Consequently, in order to improve our understanding of the important effect of MS waves on the scattering process of magnetospheric particles and resultant dynamical variations, in contrast to numerous previous observational studies that concentrated on the wave power distribution or frequency spectrum feature of MS waves, a comprehensive analysis is required to investigate in detail the WNA distribution of MS emissions, which is expected to be essential to evaluations of wave-induced diffusion effects (e.g., Shprits & Ni, 2009; Ni et al., 2013, 2015, 2019; Cao et al., 2019; Zhao et al., 2019). In the present study, the power-weighted WNAs are adopted through weighted integration over the measured magnetic power spectral density (B_{PSD}) at each frequency (f), thus representing the direction of the total wave vector in each time interval. Here, we use the data derived from Electric and Magnetic Field Instrument Suite and Integrated Science (EMFISIS; Kletzing et al., 2013) on board Van Allen Probes (Mauk et al., 2012) spanning the period from September 2012 to May 2018. The detailed methodology to identify MS waves as well as calculation of averaged power-weighted WNAs is presented in section 5. The spatial (global and latitudinal) distributions of power-weighted WNAs of MS waves at $|\lambda| \leq 15^\circ$ are shown in section 3. In section 4, we quantitatively analyze the occurrence pattern of MS waves in various WNA ranges and their detailed dependence on geomagnetic latitude, followed by the conclusions summarized in section 5.

2. Data and Methodology

Figure 1 shows an example of typical MS events observed by EMFISIS instruments on board the Van Allen Probe A spacecraft on 29 June 2013. Figure 1a illustrates the background plasma density obtained from the measurements of upper hybrid frequency (f_{UHR}), and Figures 1b–1e show the spectrogram of electric (E_{psd}) and magnetic (B_{psd}) power spectral density (PSD), the WNA, and the ellipticity, respectively. A class of intense MS waves occurs at frequencies from the proton gyrofrequency (f_{cp} , the blue dotted line) to the lower hybrid frequency (f_{UHR} , the white solid line), which are linearly polarized and propagating nearly perpendicularly to the background magnetic field with WNAs mainly larger than 80° from $\sim 11:10$ to $\sim 11:35$ UT (shaded region). During this time period, the spacecraft moves on its outbound trajectory and measured plasma density varies from $>100 \text{ cm}^3$ to $\sim 1,000 \text{ cm}^3$ (see Figure 1a), suggesting that this MS event is observed inside the PP. Here we distinguish the MS waves in each time stamp by limiting the range of WNAs from 80° to 90° and the ellipticity from -0.2 to $+0.2$ in frequencies between f_{cp} and f_{UHR} , as shown in previous studies (e.g., Ma et al., 2016; Ni et al., 2018). Only the measurement $B_{\text{PSD}}(f)$ and WNA(f) that meet this criterion will be adopted into later calculations. At each sample time (i), the MS amplitude (B_{wi}) is a function of its PSD at each frequency (f)

$$B_{\text{wi}}^2 = \int_{f_{\min}}^{f_{\max}} B_{\text{PSD}}(f) df \Big|_i. \quad (1)$$

where f_{\max} and f_{\min} are the maximum and minimum frequencies of the measured MS waves (i.e., f_{lh} and f_{cp} for MS waves), respectively. To quantitatively investigate the total propagation vector of the MS emissions at each time interval, we adopt the power-weighted or probability density function values of the WNAs, similar to Santolík et al. (2014) and Yu et al. (2017). At each sample time (i), we estimate an averaged wave normal angle ($WNA|_i$) using a weighted integration over the measured magnetic power spectral density (B_{PSD}) at each frequency (f)

$$WNA|_i = \frac{\int_{f_{\min}}^{f_{\max}} WNA(f) B_{\text{PSD}}(f) df}{\int_{f_{\min}}^{f_{\max}} B_{\text{PSD}}(f) df} \Big|_i. \quad (2)$$

Figures 1f and 1g illustrate the amplitude and power-weighted WNAs of the MS waves at each sample time, in which the MS waves become intense with $B_w > 200 \text{ pT}$ during the event time ($\sim 11:10$ to $\sim 11:35$ UT, shaded region) and WNA simultaneously varies from $\sim 82^\circ$ to 89° and dominant near $86\text{--}88^\circ$. It is noted that the

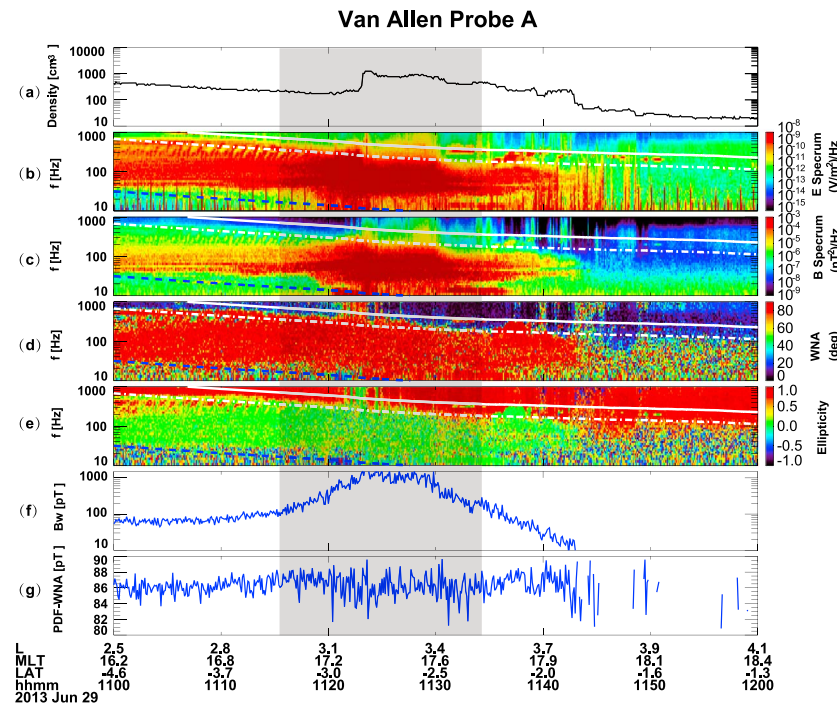


Figure 1. Overview of an example of magnetosonic (MS) events observed by Van Allen Probe A: (a) Plasma density; power spectral density of (b) the electric field (E_{PSD}) and (c) the magnetic field (B_{PSD}); (d) the wave normal angle and (e) the ellipticity. The white solid and dotted curves present lower hybrid resonant frequency (f_{LHR}) and half of lower hybrid resonant frequency ($0.5f_{\text{LHR}}$), respectively. The proton cyclotron frequency (f_{cp}) is denoted by the blue solid curve. (f) The integrated magnetic field amplitude of the off-equatorial MS waves (B_w); (g) power-weighted wave normal angles of MS waves.

weak wave powers with $B_{\text{PSD}} < 10^{-9} \text{ nT}^2/\text{Hz}$ or $B_w < 1 \text{ pT}$ are thought to be below the noise level and deleted before integrations.

Based on the same method, we use the observations from both Van Allen Probes from September 2012 to May 2018 and calculate power-weighted WNAs of all identified MS waves, to statistically obtain the storm-dependent distributions of wave amplitude and WNAs. Here, we choose AE* (1-hr averaged AE) from the Omni-Web (ftp://spdf.gsfc.nasa.gov/pub/data/omni/high_res_omni) as the indicator of geomagnetic conditions (quiet: $\text{AE}^* \leq 100 \text{ nt}$; moderate: $100 \text{ nt} \leq \text{AE}^* \leq 300 \text{ nt}$; active: $\text{AE}^* > 300 \text{ nt}$). In each bin (L , MLT, λ), the root-mean-square (RMS) wave magnetic amplitude B_w and power-weight averaged values of MS WNAs ($\langle \text{WNA} \rangle$) are obtained.

Within the statistical result, a database has been built to analyze the distributions of the magnetic amplitude of fast MS waves in Figures 2 and 3 as well as their WNAs shown in sections 5 and 6.

The global (L-MLT) and latitudinal (Lat-L) distributions of magnetic amplitude (B_w) of MS waves are shown in Figures 2 and 3. Bins with total samples less than 100 are regarded as poor statistics and removed from the database. The statistical results indicate that the MS waves with larger amplitude preferentially occur near the magnetic equator, outside the PP, on the dawnside during geomagnetically disturbed periods, which is in accordance with the previous observations (e.g., Ma et al., 2013). It is also clear that the wave amplitude can substantially decay along with increase of the geomagnetic latitude (λ) at off-equatorial region both inside and outside the PP regardless of geomagnetic activities.

3. Spatial Distributions of Power-Weighted WNAs

Figure 4 presents the global (L-MLT) distributions of WNAs (i.e., the averaged power-weighted $\langle \text{WNA} \rangle$, similarly hereinafter) of equatorial ($|\lambda| \leq 5^\circ$) and off-equatorial ($5^\circ < |\lambda| \leq 15^\circ$) MS waves both inside and outside the PP under three geomagnetic conditions (from left to right: quiet, moderate, and active). Due

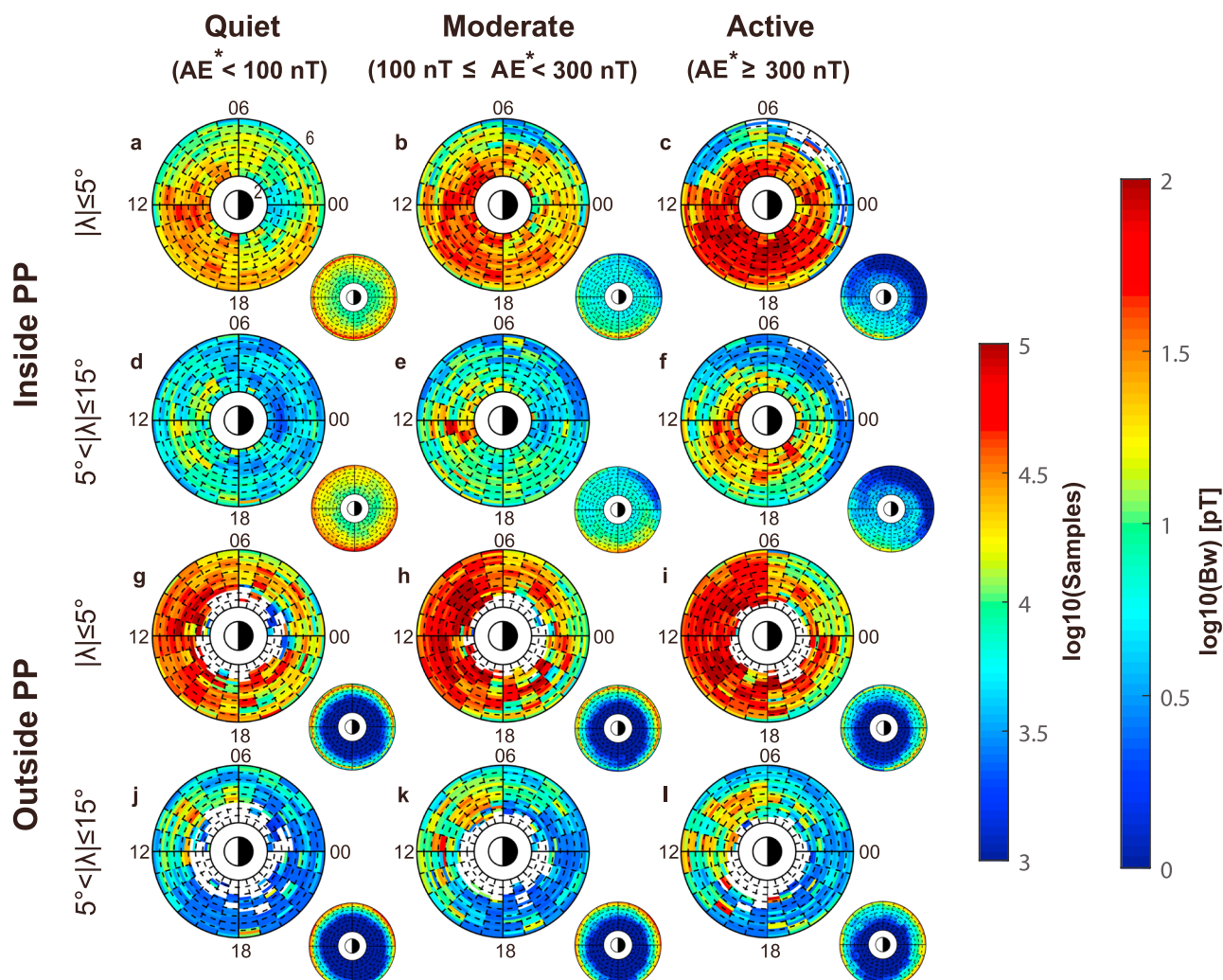


Figure 2. Global distributions (L-MLT) of averaged magnetic amplitude (B_w) of equatorial ($|\lambda| \leq 5^\circ$) and off-equatorial ($5^\circ \leq |\lambda| \leq 15^\circ$) magnetosonic waves in $L = 2-6$ inside and outside the plasmapause under three different geomagnetic activities (AE^*).

to a lack of measurements at $|\lambda| > 15^\circ$, the magnetic latitude is limited within 15° for all statistical observations in the present study. To obtain the result, the data are binned with every $0.2L$ (between $L = 2-6$) times 1 MLT hour. Bins with total samples less than 100 are regarded as poor statistics and removed from the database (e.g., some bins at $L < 3$ outside PP in Figures 4g–4l). The number of measured samples is shown in each corresponding small dial plot. Overall, it is apparent that the global WNAs are dominantly located from $\sim 87^\circ$ to $\sim 89^\circ$ in the equatorial region ($|\lambda| \leq 5^\circ$) both inside (Figures 4a–4c) and outside the PP (Figures 4g–4i) under all three geomagnetic conditions, performing a substantial feature of MS waves that propagate nearly perpendicularly with the background magnetic field line. At the off-equatorial region ($5^\circ < |\lambda| \leq 15^\circ$, Figures 4d–4f and Figures 4j–4l), however, the value of bin-averaged WNAs has a dramatic descent that fluctuates from $\sim 85^\circ$ to $\sim 86^\circ$. Therefore, it is clearly indicated that the direction of wave propagation vector of MS waves would be less perpendicular when they propagate to off-equator region.

Specifically, the overall distributions of WNAs are partly dependent on spatial location and geomagnetic activity. (1) For equatorial MS waves during quiet times (Figures 4a and 4g), the distributions of WNAs are nearly isotropic along L and MLT sector with values $\sim 88^\circ$ and have light drops at higher L-shells ($L > 4.5$) as the geomagnetic activity becomes intense (Figures 4b and 4h). During active times, the WNAs can decrease to $< 85^\circ$ on the night-to-noonside ($\sim 00-11$ MLT) at $L > \sim 5$ inside PP (Figure 4c) and decreases to

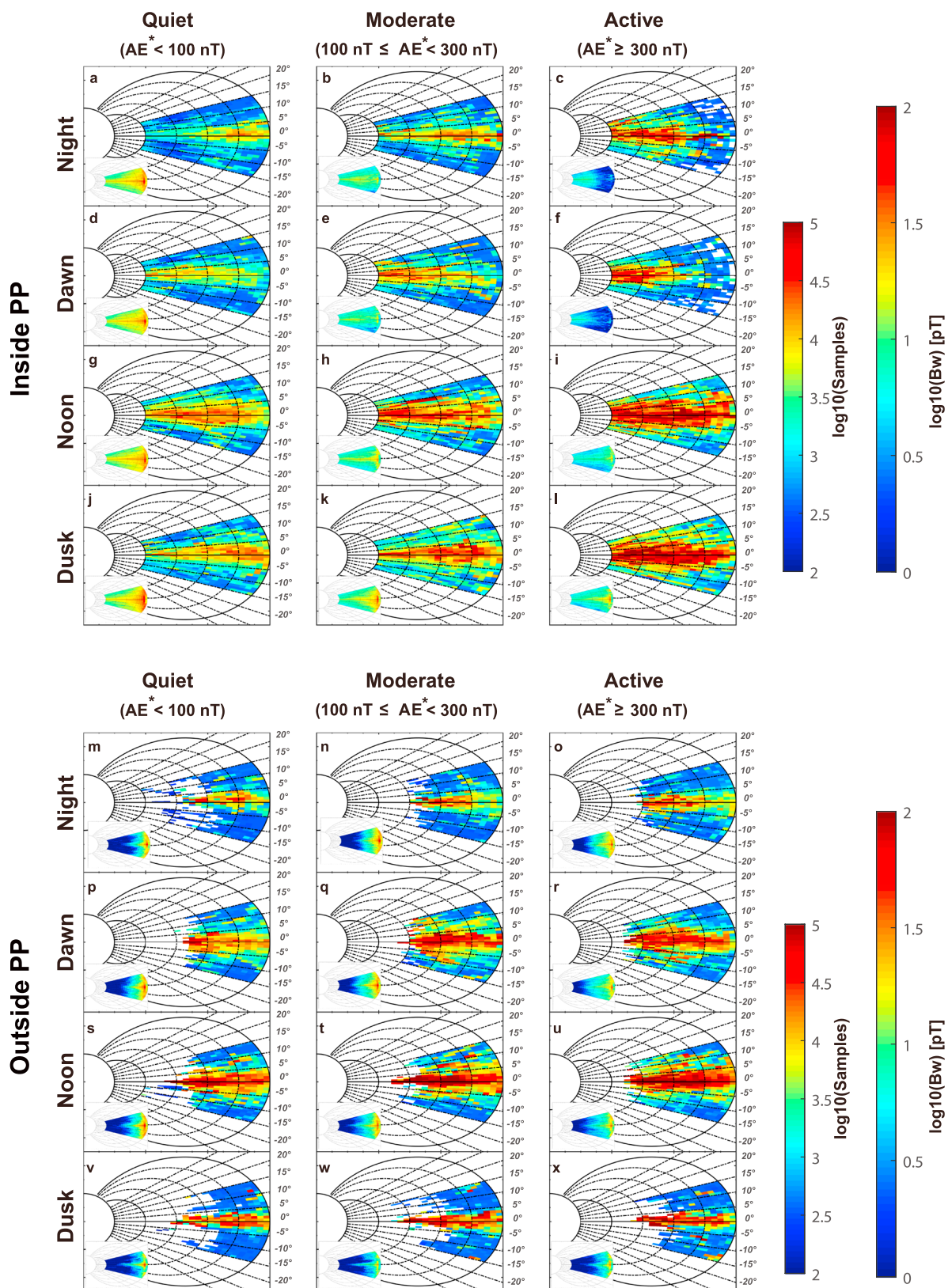


Figure 3. Latitudinal distributions (Lat-L) of averaged magnetic amplitude (B_w) of magnetosonic waves at night, dawn, noon, and dusk in $L = 2\text{--}6$ inside and outside the plasmapause under three different geomagnetic activities (AE^*).

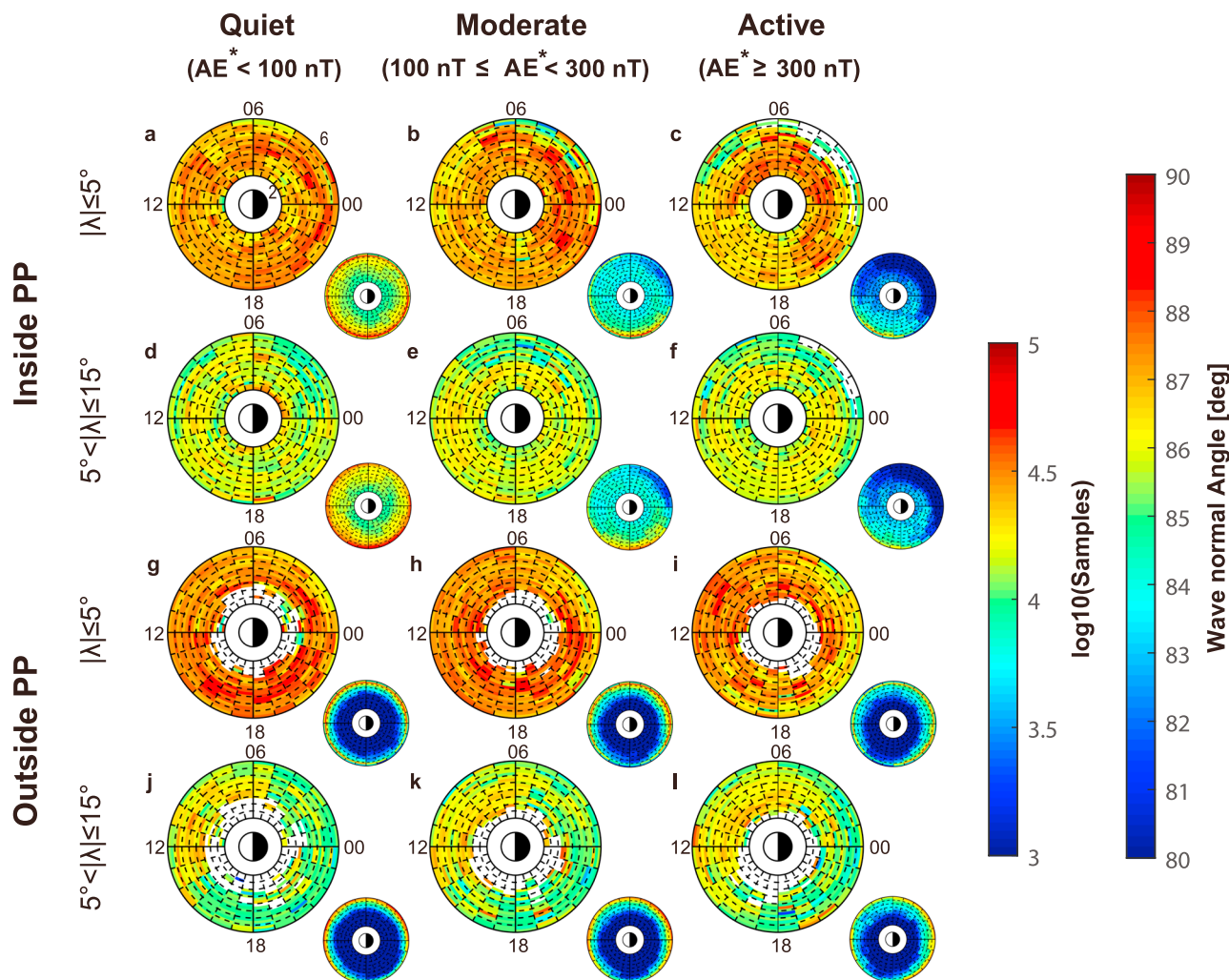


Figure 4. Global distributions (L-MLT) of power-weighted wave normal angles of equatorial ($|\lambda| \leq 5^\circ$) and off-equatorial ($5^\circ \leq |\lambda| \leq 15^\circ$) magnetosonic waves in $L = 2\text{--}6$ inside and outside the plasmapause under three different geomagnetic activities (AE^*).

86° on dusk-to-predawn (18–04 MLT) at $L > \sim 5$ outside PP (Figure 2i). (2) For off-equatorial MS waves (Figures 4d–4f and 4j–4l), the averaged WNAs are mainly located around ~86° at all MLT sectors and have a slight dependence on geomagnetic activity. In addition, the averaged WNAs of outside PP MS waves (Figures 4j–4l) in dayside (i.e., ~86°) are clearly larger than those in nightside (i.e., ~85°), showing a distinct day-night asymmetry.

Figure 5 shows the latitudinal (Lat-L) distributions of averaged power-weighted WNAs of MS waves with geomagnetic latitude (λ) ranging from -15° to 15° at four different MLT sectors (Nightside: 21–03 MLT, Dawnside: 03–09 MLT, Noonside: 09–15 MLT, and Duskside: 15–21 MLT) both inside and outside PP under three different geomagnetic conditions. The number of samples is shown in each small dial plot and the data are binned with every 0.2L (between $L = 2\text{--}6$) times every 1° latitude. As in Figure 4, bins with total samples less than 100 are also excluded. First, it is clearly illustrated that the MS waves with larger WNAs (i.e., WNA $> 87^\circ$) are dominantly confined near the magnetic equator plane ($|\lambda| \leq 5^\circ$) at all MLT sectors under all geomagnetic conditions, which is in accordance with the global observations in Figure 4. In the middle latitudes ($5^\circ < |\lambda| \leq 10^\circ$), the averaged WNAs gradually decreases to ~86°. As the latitude continues to increase, they become lower, which could be less than 85° at $|\lambda| \sim 15^\circ$. This remarkable latitudinal dependence of WNAs provides a clear evidence that the MS waves gradually become less oblique as they propagate from the Earth's magnetic equator to middle/higher latitudinal regions. Second, as the geomagnetic activity becomes intense, the value of the power-weighted WNA becomes smaller,

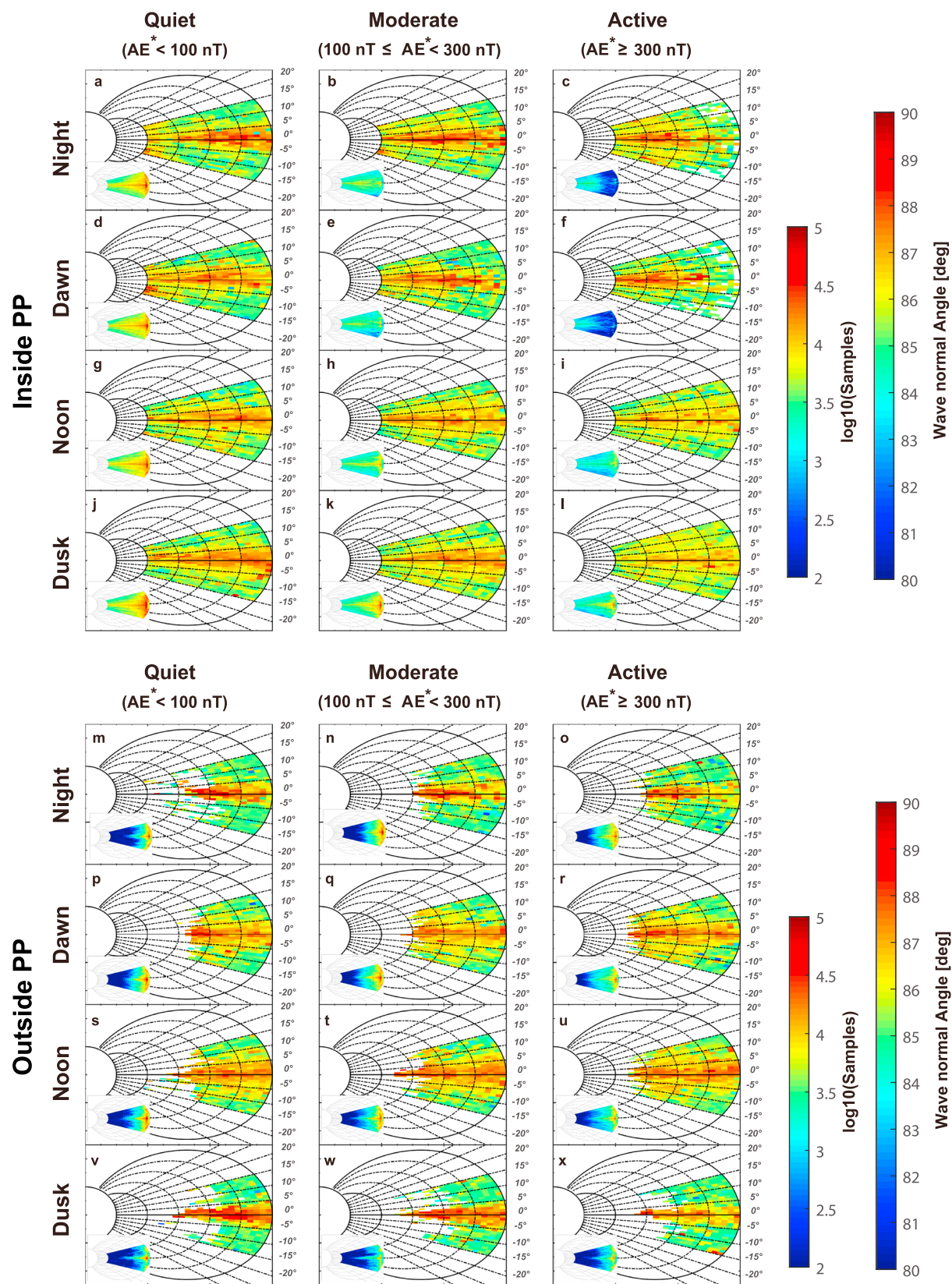


Figure 5. Latitudinal distributions (Lat-L) of power-weighted magnetosonic waves at night, dawn, noon, and dusk in $L = 2\text{--}6$ inside and outside the plasmapause under three different geomagnetic activities (AE^*).

especially at larger L-shells near magnetic equator. For example, the downside equatorial waves inside PP have WNA > 87° at $L > 5$ in geomagnetic quiet times (Figure 5d), while less obliquely propagating with WNA ~ 85° in active times (Figure 5f).

In previous simulation studies (e.g., Bortnik & Thorne, 2010; Li et al., 2014; Fu et al., 2016; Ni et al., 2018), the distribution of WNA is preferentially adopted as a Gaussian distribution with a peak around 89° or 89.5°. However, the Gaussian distribution cannot reflect the observational spatial variation of MS propagation angles (WNAs). As shown in Figures 4 and 5 the power-weighted WNAs of MS waves are dominantly located from 87–89° at the geomagnetic equatorial region and decrease with increasing geomagnetic latitude. Our statistical results provide a general view of the WNA distribution of MS waves, which can validate the related inputs of MS waves in future simulations of radiation belt particle dynamics.

4. Latitudinal Dependence of WNAs of MS Waves

To quantitatively investigate the distributions of MS WNAs in detail, the histograms have been plotted in Figures 6a–6i to show occurrence rate (ϵ) at each WNA from 80.5° to 89.5° (with resolution of 0.5°) at equatorial ($|\lambda| \leq 5^\circ$), middle latitudinal ($5^\circ < |\lambda| \leq 10^\circ$), and higher latitudinal ($5^\circ < |\lambda| \leq 15^\circ$) regions under three different geomagnetic conditions. It is distinct that the occurrence rate in each subplot gradually varies along with the WNAs and act as a one-peak distribution. Here we fit the statistical result in each subplot with a red solid curve by a mixture of two Gaussian distributions

$$\epsilon = A_1 e^{-\left(\frac{WNA - \mu_1}{\sigma_1}\right)^2} + A_2 e^{-\left(\frac{WNA - \mu_2}{\sigma_2}\right)^2}, \quad (3)$$

where A_1 , A_2 , μ_1 , μ_2 , σ_1 , σ_2 denote the corresponding Gaussian-fitted coefficients, which are listed in Table 1a. The location of peak WNA and the value of related occurrence rates are also marked, respectively, with red vertical and horizontal dotted lines. In order to show the dispersion of the distribution, we set the lower and upper locations with occurrence rate half of the peak value, for example, 83.8° and 89.4° in Figure 6a, as are marked with red vertical dotted lines in each subplot. Note that the upper locations in Figures 6d, 6e, and 6g–6i are not shown since no occurrence rates are smaller than the half of the peak values. Generally, it is interesting that the fitted curve can well trace the outline of the occurrence rate in each subplot, indicating that the angle between the wave-propagated vector of MS waves and the ambient geomagnetic field line substantially distributes as a mixture of two Gaussian distributions along with values of WNA, regardless of different latitudes and various geomagnetic activities. As geomagnetic storm intensity (Figures 6b, 6c, 6e, 6f, 6h, and 6i), the configuration of occurrence curves at all latitudes become sharper while the location of the peak WNA remains relatively unchanged, for example, the upper and lower locations of WNAs for equatorial MS waves are located at 83.8° and 89.4° in quiet times while 84.4° and 89.1° in active times.

For equatorial MS waves in quiet times (see Figure 6a), the occurrence rate varies more steeply at the range from ~85° to 89.5° than at other WNAs and peaks at 87.3° with $\epsilon = 8.6\%$ and the lower/upper locations at 83.8°/84.4°, thus showing a “steepletop” distribution. At middle (Figure 6d) and higher (Figure 6g) latitudes, the occurrence rate is comparatively flatter with slightly lower peaks about $\epsilon = 6.2\%$ at WNA = 86.4° and $\epsilon = 5.7\%$ at WNA = 86.0° as well as the lower and upper locations at <81° and >89.1°, respectively. It is also indicated that much lower WNAs (< ~85°) of MS waves occur with the increase of geomagnetic latitude, for example, the waves with WNA = 80.5° counts <2.5% near the equator, while can up to ~3% or larger at middle and higher latitudes.

Figures 6j–6u show the distributions of averaged power-weighted WNAs as a function of geomagnetic latitude (λ) at $L = 3–6$ under three different geomagnetic conditions. Each bin of MLAT in every histogram covers 0.5°. It is obvious that the total trend of the averaged WNAs at $L = 3–5$ (Figures 6j–6r) gradually decreases as λ increases in each L-shell and geomagnetic condition, with the value from >87° near the magnetic equator to about or less than 86° at $\lambda > \sim 10^\circ$. At $L = 6$, however, the outline of the values shows larger gradient, where the averaged WNAs could be as low as 85° in quiet times and even 84° in moderate times at $\lambda > \sim 10^\circ$. This is in accordance with the result in Figures 4 and 5. In order to quantitatively show the detailed latitudinal dependence of WNAs of MS waves, we fit the statistical result with red solid curves by a Kappa distribution function

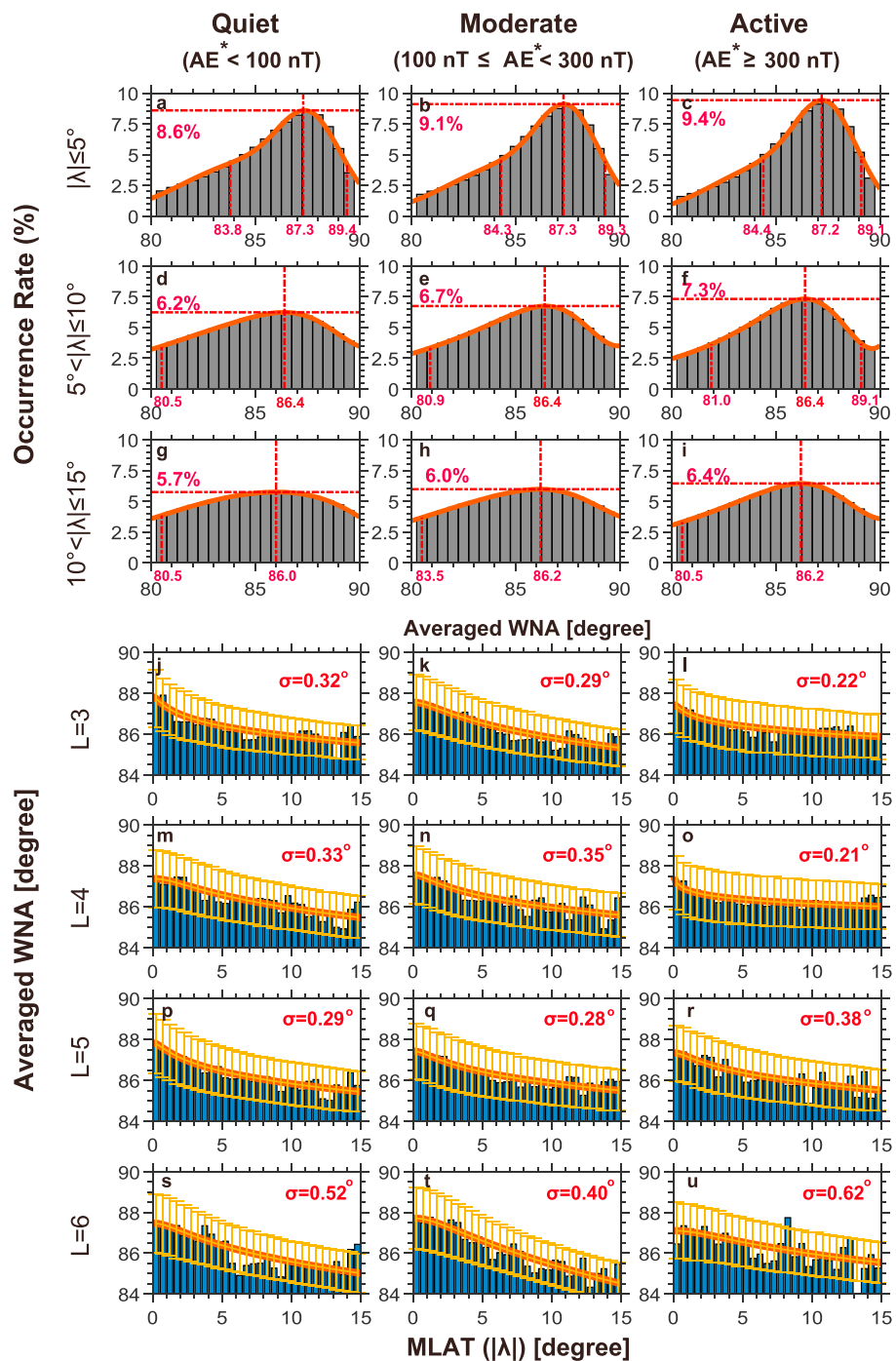


Figure 6. Histograms of (a) occurrence rate of power-weighted wave normal angles (WNAs) at three latitudinal regions; (b) averaged power-weighted WNA distribution by geomagnetic latitude (λ) at $L = 3\text{--}6$ under three different geomagnetic activities (AE^*).

$$\tan(\text{WNA}) = C \left(1 + \frac{\lambda}{\kappa t}\right)^{-(1+\kappa)} \quad (4)$$

C , κ , and t denote the fitted coefficients that are listed in Table 1b. In order to quantitatively show the WNA distribution at different MLAT sectors, the y axis is set as WNA itself rather than $\tan(\text{WNA})$. That means the red curve in each subplot means $\arctan(C(1 + \frac{\lambda}{\kappa t})^{-(1+\kappa)})$. The error bars between the fitted result and

Table 1

Fitted Coefficients of (a) Occurrence Rate of Power-Weighted WNAs at Three-Latitudinal Regions; (b) Averaged Power-Weighted WNA Distribution by Geomagnetic Latitude (λ) at $L = 3\text{--}6$ Under Three Different Geomagnetic Activities (AE^*)

	Quiet	Moderate	Active		
(a) Occurrence rate (%)					
$ \lambda \leq 5^\circ$	$A_1 = 4.2749;$ $\mu_1 = 84.6263;$ $\sigma_1 = 4.4255;$	$A_2 = 5.7982;$ $\mu_2 = 87.6626;$ $\sigma_2 = 2.0889;$	$A_1 = 4.0604;$ $\mu_1 = 84.6665;$ $\sigma_1 = 4.1684;$	$A_2 = 6.4959;$ $\mu_2 = 87.5788;$ $\sigma_2 = 2.0833;$	$A_1 = 3.9782;$ $\mu_1 = 84.6795;$ $\sigma_1 = 3.9537$
$5^\circ < \lambda \leq 10^\circ$	$A_1 = 7.3022;$ $\mu_1 = 89.9935;$ $\sigma_1 = 11.0284;$	$A_2 = -4.0705;$ $\mu_2 = 90.6502;$ $\sigma_2 = 2.6909;$	$A_1 = 25.0368;$ $\mu_1 = 104.7300$	$A_2 = -8.3614;$ $\mu_2 = 90.4862;$ $\sigma_2 = 2.7132;$	$A_1 = 7.5048;$ $\mu_1 = 89.3354;$ $\sigma_1 = 11.2743;$
$5^\circ < \lambda \leq 15^\circ$	$A_1 = 5.7724;$ $\mu_1 = 86.2695;$ $\sigma_1 = 9.0485;$	$A_2 = -2.3746;$ $\mu_2 = 92.6448;$ $\sigma_2 = 3.1159;$	$A_1 = 6.4601;$ $\mu_1 = 88.2786;$ $\sigma_1 = 10.3458;$	$A_2 = -2.6825;$ $\mu_2 = 90.7332;$ $\sigma_2 = 2.8882;$	$A_1 = 13.6711;$ $\mu_1 = 97.6283;$ $\sigma_1 = 14.3827;$
(b) WNA (degree)					
$L = 3$	$C = 26.2803;$ $t = -0.1328;$	$\kappa = -0.9056;$	$C = 23.3989;$ $t = -2.7493;$	$\kappa = -0.8576;$	$C = 22.3419;$ $t = -0.0983;$
$L = 4$	$C = 21.7888;$ $t = -4.9356;$	$\kappa = -0.8630;$	$C = 23.4935;$ $t = -1.1785;$	$\kappa = -0.8894;$	$C = 23.5235;$ $t = -0.0017;$
$L = 5$	$C = 26.3079;$ $t = -0.3929;$	$\kappa = -0.8853;$	$C = 22.2420;$ $t = -1.2365;$	$\kappa = -0.8946;$	$C = 21.4869;$ $t = -1.2303;$
$L = 6$	$C = 22.6988;$ $t = -3.1782;$	$\kappa = -0.8459;$	$C = 25.1780;$ $t = -7.9024;$	$\kappa = -0.7575;$	$C = 19.8097;$ $t = -10.3015;$

observations in every 0.5° of latitude are shown in each subplot. It is indicated that the WNAs are mainly distributed around the Kappa distribution curve with RMS $\sim 1^\circ$. In addition, we also adopt the total root-mean-square deviation (RMSD) σ between the fitted WNAs and the averaged observations as the indicator of the goodness of the fit, which is also marked with the red color in each subplot.

$$\sigma = \sqrt{\frac{\sum_{i=1}^n (WNA_{\text{fit}} - WNA_{\text{average}})^2}{n}} \quad (5)$$

WNA_{fit} , WNA_{average} , and n show the fitted result, the original value to fit and the total number of fitted WNAs. Overall, the fitted curves could almost capture the outlines of histograms for all subplots with the value of fitted RMSD σ that varies from $\sim 0.2^\circ$ to $\sim 0.6^\circ$, which means that the fitting can reproduce the averaged WNA with an error less than 0.6° . Therefore, it is clearly indicated that the Kappa distribution function could well fit the tangent of MS waves along geomagnetic latitude (λ) at multiple L -shells. Specifically, compared with the values less than 0.4 at $L = 3\text{--}5$, the fitted RMSD σ are much larger at $L = 6$, especially in active time, in which it is as large as 0.62. Apparently, there are some fluctuations of the averaged WNAs happening as λ grows at $L = 6$, for example, a positive pulse occurs in $\lambda \sim 8.5$ with WNA $\sim 88^\circ$ at $L = 6$, which may reduce the goodness of fit.

With the well fit of distributions of occurrence outlines by a mixture of two Gaussian distributions by WNAs as well as the tangent of WNAs by Kappa distribution function (see Figure 6), we give quantitative dependence of MS WNAs in detail, thus providing brief and reasonable empirical models to estimate the values of MS WNAs at multiple spatial locations.

5. Conclusions

Based on observations from EMFISIS instruments on board both Van Allen Probes spacecraft, we have focused on the distribution of power-weighted WNA, which is evaluated through weighted integration over the measured magnetic power spectral density (B_{PSD}) at each wave frequency (f). With the availability of over 68 months of data (power-weighted) during the period from September 2012 to May 2018, we have statistically investigated the global spatial distributions of WNA of MS waves within $|\lambda| = 15^\circ$ at $L = 2\text{--}6$ and all MLT sectors in the plasmasphere and trough region under geomagnetically quiet, moderate, and active

conditions. Further quantitative dependence of the MS wave occurrence rate at different WNAs and of the bin-averaged WNAs on geomagnetic latitude have also been analyzed at multiple L-shells.

The major conclusions are summarized as follow:

1. Power-weighted WNAs of MS waves are dominantly located within 87–89° at the geomagnetic equatorial region and can be as low as ~85° at higher latitudes.
2. The WNAs of MS waves are distributed as a mixture of two Gaussian distributions and the tangent of it decreases as a Kappa distribution function with increasing geomagnetic latitude.
3. The spatial (global and latitudinal) distribution of WNAs (power-weighted) and their quantitatively fitted dependence on λ , L-shell, and geomagnetic condition is now available for incorporation into future global simulations of radiation belt electron dynamics that require to reasonably take into account the scattering effect of fast magnetosonic waves.

Acknowledgments

This work was supported by the NSFC grants 41674163, 41474141, 41574160, 41704162, and 41731067, Shenzhen Technology Project JCYJ20170307150645407, and the Hubei Province Natural Science Excellent Youth Foundation (2016CFA044). The EMFISIS data are obtained from <https://emfisis.physics.uiowa.edu/data/index>. The data of geomagnetic indices are available from the NASA OmniWeb (<http://cdaweb.gsfc.nasa.gov>).

References

- Artemyev, A. V., Mourenas, D., Agapitov, O. V., & Krasnoselskikh, V. V. (2015). Relativistic electron scattering by magnetosonic waves: Effects of discrete wave emission and high wave amplitudes. *Physics of Plasmas*, 22(6), 062901. <https://doi.org/10.1063/1.4922061>
- Balikhin, M. A., Shprits, Y. Y., Walker, S. N., Chen, L., Cornilleau-Wehrlin, N., Dandouras, I., et al. (2015). Observations of discrete harmonics emerging from equatorial noise. *Nature Communications*, 6(1). <https://doi.org/10.1038/ncomms8703>
- Boardsen, S. A., Hospodarsky, G. B., Kletzing, C. A., Pfaff, R. F., Kurth, W. S., Wygant, J. R., & MacDonald, E. A. (2014). Van Allen Probe observations of periodic rising frequencies of the fast magnetosonic mode. *Geophysical Research Letters*, 41, 8161–8168. <https://doi.org/10.1002/2014GL062020>
- Bortnik, J., & Thorne, R. M. (2010). Transit time scattering of energetic electrons due to equatorially confined magnetosonic waves. *Journal of Geophysical Research*, 115(A7), A07213. <https://doi.org/10.1029/2010JA015283>
- Cao, X., Ni, B., Summers, D., Shprits, Y. Y., Gu, X., Fu, S., et al. (2019). Sensitivity of EMIC wave-driven scattering loss of ring current protons to wave normal angle distribution. *Geophysical Research Letters*, 46(2), 590–598. <https://doi.org/10.1029/2018GL081550>
- Chen, L., & Thorne, R. M. (2012). Perpendicular propagation of magnetosonic waves. *Geophysical Research Letters*, 39, L14102. <https://doi.org/10.1029/2012GL052485>
- Fu, H. S., Cao, J. B., Zhima, Z., Khotyaintsev, Y. V., Angelopoulos, V., Santolik, O., & Huang, S. Y. (2014). First observation of rising-tone magnetosonic waves. *Geophysical Research Letters*, 41, 7419–7426. <https://doi.org/10.1002/2014GL061867>
- Fu, S., Ni, B., Li, J., Zhou, C., Gu, X., Huang, S., et al. (2016). Interactions between magnetosonic waves and ring current protons: Gyroaveraged test particle simulations. *Journal of Geophysical Research: Space Physics*, 121, 8537–8553. <https://doi.org/10.1002/2016JA023117>
- Horne, R. B., Thorne, R. M., Glauert, S. A., Meredith, N. P., Pokhotelov, D., & Santolik, O. (2007). Electron acceleration in the Van Allen radiation belts by fast magnetosonic waves. *Geophysical Research Letters*, 34, L17107. <https://doi.org/10.1029/2007GL030267>
- Hua, M., Ni, B., Li, W., Gu, X., Fu, S., Shi, R., et al. (2019). Evolution of radiation belt electron pitch angle distribution due to combined scattering by plasmaspheric hiss and magnetosonic waves. *Geophysical Research Letters*, 46, 3033–3042. <https://doi.org/10.1029/2018GL081828>
- Kletzing, C. A., Kurth, W. S., Acuna, M., MacDowall, R. J., Torbert, R. B., Averkamp, T., et al. (2013). The Electric and Magnetic Field Instrument Suite and Integrated Science (EMFISIS) on RBSP. *Space Science Reviews*, 179(1–4), 127–181. <https://doi.org/10.1007/s11214-013-9993-6>
- Lei, M., Xie, L., Li, J., Pu, Z., Fu, S., Ni, B., et al. (2017). The radiation belt electron scattering by magnetosonic wave: Dependence on key parameters. *Journal of Geophysical Research: Space Physics*, 122, 12,338–12,352. <https://doi.org/10.1002/2016JA023801>
- Li, J., Bortnik, J., Li, W., Ma, Q., Thorne, R. M., Kletzing, C. A., et al. (2017). “Zipper-like” periodic magnetosonic waves: Van Allen Probes, THEMIS, and magnetospheric multiscale observations. *Journal of Geophysical Research: Space Physics*, 122, 1600–1610. <https://doi.org/10.1002/2016JA023536>
- Li, J., Ni, B., Xie, L., Pu, Z., Bortnik, J., Thorne, R. M., et al. (2014). Interactions between magnetosonic waves and radiation belt electrons: Comparisons of quasi-linear calculations with test particle simulations. *Geophysical Research Letters*, 41, 4828–4834. <https://doi.org/10.1029/2014GL060461>
- Ma, Q., Li, W., Thorne, R. M., & Angelopoulos, V. (2013). Global distribution of equatorial magnetosonic waves observed by THEMIS. *Geophysical Research Letters*, 40, 1895–1901. <https://doi.org/10.1002/grl.50434>
- Ma, Q., Li, W., Thorne, R. M., Bortnik, J., Kletzing, C. A., Kurth, W. S., & Hospodarsky, G. B. (2016). Electron scattering by magnetosonic waves in the inner magnetosphere. *Journal of Geophysical Research: Space Physics*, 121, 274–285. <https://doi.org/10.1002/2015JA021992>
- Mauk, B. H., Fox, N. J., Kanekal, S. G., Kessel, R. L., Sibeck, D. G., & Ukhorskiy, A. (2012). Science objectives and rationale for the Radiation Belt Storm Probes mission. *Space Science Reviews*, 179, 3–27. <https://doi.org/10.1007/s11214-012-9908-y>
- Meredith, N. P., Horne, R. B., & Anderson, R. R. (2008). Survey of magnetosonic waves and proton ring distributions in the Earth's inner magnetosphere. *Journal of Geophysical Research*, 113, A06213. <https://doi.org/10.1029/2007JA012975>
- Mourenas, D., Artemyev, A. V., Agapitov, O. V., & Krasnoselskikh, V. (2013). Analytical estimates of electron quasi-linear diffusion by fast magnetosonic waves. *Journal of Geophysical Research: Space Physics*, 118, 3096–3112. <https://doi.org/10.1002/jgra.50349>
- Ni, B., Bortnik, J., Thorne, R. M., Ma, Q., & Chen, L. (2013). Resonant scattering and resultant pitch angle evolution of relativistic electrons by plasmaspheric hiss. *Journal of Geophysical Research: Space Physics*, 118, 7740–7751. <https://doi.org/10.1002/2013JA019260>
- Ni, B., Cao, X., Zou, Z., Zhou, C., Gu, X., Bortnik, J., et al. (2015). Resonant scattering of outer zone relativistic electrons by multi-band EMIC waves and resultant electron loss timescales. *Journal of Geophysical Research: Space Physics*, 120, 7357–7373. <https://doi.org/10.1002/2015JA021466>
- Ni, B., Hua, M., Zhou, R., Yi, J., & Fu, S. (2017). Competition between outer zone electron scattering by plasmaspheric hiss and magnetosonic waves. *Geophysical Research Letters*, 44, 3465–3474. <https://doi.org/10.1002/2017GL072989>
- Ni, B., Huang, H., Zhang, W., Gu, X., Zhao, H., Li, X., et al. (2019). Parametric sensitivity of the formation of reversed electron energy spectrum caused by plasmaspheric hiss. *Geophysical Research Letters*, 46, 4134–4143. <https://doi.org/10.1029/2019GL082032>

- Ni, B., Zou, Z., Fu, S., Cao, X., Gu, X., & Xiang, Z. (2018). Resonant scattering of radiation belt electrons by off-equatorial magnetosonic waves. *Geophysical Research Letters*, 45, 1228–1236. <https://doi.org/10.1002/2017GL075788>
- Russell, C. T., Holzer, R. E., & Smith, E. J. (1970). OGO 3 observations of ELF noise in the magnetosphere: 2. The nature of the equatorial noise. *Journal of Geophysical Research*, 75(4), 755–768. <https://doi.org/10.1029/JA075i004p00755>
- Santolík, O., Macúšová, E., Kolmašová, I., Cornilleau-Wehrlin, N., & de Conchy, Y. (2014). Propagation of lower-band whistler-mode waves in the outer Van Allen belt: Systematic analysis of 11 years of multi-component data from the Cluster spacecraft. *Geophysical Research Letters*, 41, 2729–2737. <https://doi.org/10.1002/2014GL059815>
- Santolík, O., Pickett, J. S., Gurnett, D. A., Maksimovic, M., & Cornilleau-Wehrlin, N. (2002). Spatiotemporal variability and propagation of equatorial noise observed by Cluster. *Journal of Geophysical Research*, 107(A12), SMP 43-1–SMP 43-8. <https://doi.org/10.1029/2001JA009159>
- Shprits, Y. Y., & Ni, B. (2009). Dependence of the quasi-linear scattering rates on the wave normal distribution of chorus waves. *Journal of Geophysical Research*, 114, A11205. <https://doi.org/10.1029/2009JA014223>
- Shprits, Y. Y., Runov, A., & Ni, B. (2013). Gyro-resonant scattering of radiation belt electrons during the solar minimum by fast magnetosonic waves. *Journal of Geophysical Research: Space Physics*, 118, 648–652. <https://doi.org/10.1002/jgra.50108>
- Tsurutani, B. T., Falkowski, B. J., Pickett, J. S., Verkhoglyadova, O. P., Santolík, O., & Lakhina, G. S. (2014). Extremely intense ELF magnetosonic waves: A survey of polar observations. *Journal of Geophysical Research: Space Physics*, 119, 964–977. <https://doi.org/10.1002/2013JA019284>
- Xiao, F., Zhou, Q., He, Y., Yang, C., Liu, S., Baker, D. N., et al. (2015). Penetration of magnetosonic waves into the plasmasphere observed by the Van Allen Probes. *Geophysical Research Letters*, 42, 7287–7294. <https://doi.org/10.1002/2015GL065745>
- Yu, J., Li, L. Y., Cao, J. B., Chen, L., Wang, J., & Yang, J. (2017). Propagation characteristics of plasmaspheric hiss: Van Allen Probe observations and global empirical models. *Journal of Geophysical Research: Space Physics*, 122, 4156–4167. <https://doi.org/10.1002/2016JA023372>
- Zhao, H., Ni, B., Li, X., Baker, D. N., Johnston, W., Zhang, W., et al. (2019). Plasmaspheric hiss waves generate a reversed energy spectrum of radiation belt electrons. *Nature Physics*, 15, 367–372. <https://doi.org/10.1038/s41567-018-0391-6>